Proceedings of the ASME 2012 Internal Combustion Engine Division Fall Technical Conference
ICEF2012
September 23-26, 2012, Vancouver, BC, Canada

ICEF2012-92043

GRID-CONVERGENT SPRAY MODELS FOR INTERNAL COMBUSTION ENGINE CFD SIMULATIONS

P. K. Senecal
Convergent Science, Inc.
Middleton, WI, USA

E. Pomraning
Convergent Science, Inc.
Middleton, WI, USA

K. J. Richards
Convergent Science, Inc.
Middleton, WI, USA

S. Som
Argonne National Laboratory
Argonne, IL, USA

ABSTRACT

A state-of-the-art spray modeling methodology is presented. Key features of the methodology, such as Adaptive Mesh Refinement (AMR), advanced liquid-gas momentum coupling, and improved distribution of the liquid phase, are described. The ability of this approach to use cell sizes much smaller than the nozzle diameter is demonstrated. Grid convergence of key parameters is verified for non-evaporating, evaporating, and reacting spray cases using cell sizes down to 1/32 mm. Grid settings are recommended that optimize the accuracy/runtime tradeoff for RANS-based spray simulations.

INTRODUCTION

Historically, Lagrangian droplet models have been extensively used to simulate internal combustion engine sprays due to their relative ease of implementation and low simulation times. Although these models are widely used, many researchers have reported a strong dependency of spray characteristics on grid size. This large grid size dependency makes it difficult for modelers to know ahead of time what cell size to utilize. As a result, it is unknown if errors in engine simulation results are caused by input uncertainties, deficiencies in sub-models, or simply because the spray was under-resolved.

To overcome the grid dependency issue for coarse grids, Yang et al. [1, 2] developed a Relative Velocity Correction (RVC) model based on the theory of steady turbulent gas-jet flow. With this approach, a set of empirical equations was used to determine the gas-phase velocity along the spray axis and modify the relative velocity between the gas and liquid phases. Improvements in spray penetration for coarse grids were obtained with the RVC model compared to direct coupling with the CFD velocity field.

It is important to note that the model of Yang et al. was proposed over a decade ago, when coarse mesh simulations were standard practice due to serial engine codes (i.e., KIVA-3V) and slow CPU speeds compared to today's processors. As a result, such a model allowed researchers to obtain reasonable global spray behavior for coarse grids by introducing additional empiricism into the simulations.

More recently, a similar gas-jet model was introduced by Abani et al. [3], who reported that good agreement with experimental penetration was not achieved with the standard KIVA momentum coupling and collision models. In addition, as the mesh was refined, the spray behavior did not converge using the standard models. On the other hand, use of the proposed gas-jet model resulted in virtually identical liquid penetration results for cell sizes between 0.25 mm and 4 mm.

The fact that models based on gas-jet theory have been shown to result in grid independent spray penetration can make it very tempting to run coarse grids in engine simulations. However, even though the liquid penetration is captured, use of a coarse grid will under-resolve the flow field, potentially leading to inaccuracies in mixing and combustion. Furthermore, the gas-jet model is zeroth order and hence may not be predictive for arbitrary flows. In the age of parallel CFD solvers and ever-increasing CPU speeds, it is the authors' opinion that modern engine simulations should rely on enhanced mesh resolution to accurately represent the appropriate physics in sprays.

This paper takes a different approach to achieving grid independent spray results from the gas-jet models described above. Instead of employing a technique that is insensitive to the mesh size, the goal of this study is to develop a model in which the spray characteristics of interest asymptotically converge as the mesh is refined (called here "grid convergence"

 Copyright © 2012 by ASME

and not "grid independence"). The current approach has the correct behavior that under-resolved coarse mesh simulations produce inaccurate results, while refining the mesh converges to the correct solution. A similar strategy was presented by Lippert et al. [4], however that study only examined cell sizes down to 0.7 mm for relatively low injection pressure sprays. To the authors' knowledge, the present work is the first study to demonstrate grid convergence down to cell sizes on the order of 30 microns (i.e., 1/32 mm) for high pressure sprays.

To validate the current technique, non-vaporizing, vaporizing, and reacting sprays are simulated and compared to available experimental data. Future studies will involve grid convergence investigations for full-cycle 3D engine simulations as well. It is shown that reasonable grid convergence is obtained for the quantities of interest. Because convergence is achieved, it is possible to make recommendations on cell sizes that optimize the accuracy/runtime tradeoff. Although the engine modeling community will greatly benefit from the availability of this information, it is important to keep in mind that it is only applicable when a grid-convergent computational methodology is employed.

COMPUTATIONAL METHODOLOGY

In this work, the CONVERGE CFD software package [5, 6] is used as the computational framework for running the spray and combustion simulations. CONVERGE is a general purpose CFD code for the calculation of three-dimensional, incompressible or compressible, chemically-reacting fluid flows in complex geometries with stationary or moving boundaries. CONVERGE can handle an arbitrary number of species and chemical reactions, as well as transient liquid sprays, and laminar or turbulent flows. CONVERGE uses an innovative modified cut-cell Cartesian method that eliminates the need for the computational grid to be morphed with the geometry of interest while still precisely representing the true boundary shape. This approach allows for the use of simple orthogonal grids and completely automates the mesh generation process.

This section presents a brief overview of the mesh manipulation, numerical algorithms, and physical sub-models used in the current work as these elements all contribute to the grid convergence behavior achieved.

Fixed Grid Embedding

It is often desirable to add grid resolution locally in critical flow sections of the domain while leaving less critical sections relatively coarse. For example, in the present work, extra grid resolution was added to resolve the complex flow behavior at the nozzle exit, while leaving the remaining grid coarse to minimize simulation time. It is important to note that fixed embedding is specified in a small volume close to the nozzle and is only meant to seed the adaptive mesh refinement described below.

Adaptive Mesh Refinement

In most cases, it is difficult to determine *a priori* where fixed grid embedding should be added. In these cases, Adaptive Mesh Refinement (AMR) can be applied. Ideally, a good AMR algorithm should add embedding where the flow field is most under-resolved or where the sub-grid field is the largest. CONVERGE estimates the magnitude of the sub-grid field to determine where embedding is added.

For a scalar, the sub-grid field is defined as the difference between the actual field and the resolved field or

$$f' = f - \overline{f} \,, \tag{1}$$

where f is the actual scalar field, $\overline{f}$ is the resolved scalar field and f' is the sub-grid scalar field. The sub-grid for any scalar can be expressed as an infinite series [7, 8, 9]. Since it is not possible to evaluate the entire series, only the first term (the 2nd order term) in the series is used to approximate the scale of the sub-grid or

$$f' \cong -\alpha_{[k]} \frac{\partial^2 \overline{f}}{\partial x_k \partial x_k} \tag{2}$$

where $\alpha_{[k]}$ is $dx_k^2/24$ for a rectangular cell and the brackets, [], indicate no summation.

A cell is embedded if the absolute value of the sub-grid is above a user specified value. Conversely, a cell is "released" (i.e., the embedding is removed) if the absolute value of the sub-grid is below a user specified value. To limit the number of embedded cells, a maximum overall number of cells can be specified by the user. With this feature, the user can specify the total number of cells desired in the simulation and AMR will determine where to put the embedding to both best resolve the flow field and meet the target number of cells.

In the present work, AMR is used for the velocity field for the non-evaporating and evaporating spray cases. AMR is used for both the velocity and temperature fields for the reacting cases. As the current study includes grid sizes down to 1/32 mm (i.e., 0.03125 mm), it is critical to include AMR in order to capture important flow features without requiring unrealistically large cell counts.

The results that follow reference minimum cell sizes, dx, and their corresponding embed scales. These two parameters are related through the base grid cell size, dx_{base}, according to the expression

$$dx = dx_{base} \times 2^{-(embed\ scale)} \tag{3}$$

For example, for a base grid cell size of 2 mm, an embed scale of 3 corresponds to a dx of 0.25 mm.

Copyright © 2012 by ASME

Numerical Algorithms

In CONVERGE, all computed values are collocated at the center of the computational cell. To prevent checker-boarding, the Rhie-Chow [10] algorithm is employed. The conservation equations are solved using the finite volume method.

In the present study a second order accurate spatial discretization scheme is used for the governing conservation equations. In order to maintain stability, time accuracy is set to first order by running fully implicit.

The transport equations are solved using the Pressure Implicit with Splitting of Operators (PISO) method of Issa [11]. A geometric multigrid solver is used for the pressure solution.

Variable time-stepping is used in the current study. The time-step is automatically calculated each computational cycle based on maximum allowed CFL numbers as well as spray, evaporation and combustion time-step control methods.

The simulations in this study are run in parallel on distributed memory machines using the Message Passing Interface (MPI). CONVERGE includes an automatic domain decomposition technique which allows for efficient load balancing throughout the calculation as the distribution of cells can change significantly due to AMR.

Physical Sub-Models

CONVERGE includes state-of-the-art models for turbulence, spray injection, liquid drop dynamics, and combustion of hydrocarbon fuels. This section provides a brief overview of the sub-models that were used in the present study. A much more detailed description of the models is given in [5].

The present study utilizes the RNG $k-\varepsilon$ model [12] to simulate turbulence. As a result, the conclusions presented in this work are only applicable to RANS-based simulations.

Accurate predictions of spray droplet dynamics and breakup are essential for modeling the subsequent vaporization, ignition, and combustion phenomena. The present simulations employ the "blob" injection method of Reitz and Diwakar [13] in which "parcels" of liquid with a characteristic size equal to the effective nozzle diameter are injected into the computational domain. The atomization of the liquid blobs and subsequent droplets is simulated with models based on the Kelvin-Helmholtz (KH) and Rayleigh-Taylor (RT) instability mechanisms without the use of a breakup length [6].

The No Time Counter (NTC) collision method of Schmidt and Rutland [14] is used in the present simulations. In general, the NTC model has a computational cost that is linear with the number of spray parcels, while traditional models have a cost that increases with the square of the number of parcels. As a result, the NTC model allows for a better statistical representation of a spray since more parcels can be used for a given amount of injected fuel. When collision occurs, the outcome is predicted to be bouncing, stretching separation, reflexive separation, or coalescence based on the conditions at impact [15].

In addition to the breakup and collision models described above, models are also included for drop drag [16] and drop turbulent dispersion [17]. These models are adequately described in the literature and thus are not described here.

A single component vaporization model, similar to the one described in [17], was used in the present calculations. The basis of this model is the Frossling correlation which calculates the time rate of change of drop radius based on the laminar mass diffusivity of the fuel vapor, a mass transfer number, and a Sherwood number.

The SAGE detailed chemistry solver [18] is used for the reacting cases in the current study. A reduced n-heptane chemical mechanism including 42 species and 168 reversible reactions is used [19]. This mechanism has been previously validated by Nordin [19] for engine applications and Senecal et al. [18] for flame lift-off and engine simulations.

Approach to Achieving Grid Convergence

This section summarizes the key elements of the computational methodology that result in the grid convergent behavior demonstrated below. Specifically, the following items are critical to achieving grid convergence:

1. *Adaptive Mesh Refinement (AMR)* – Demonstration of grid convergence can only be accomplished if cell sizes below the point of convergence can be simulated. AMR allows the use of a very fine grid in the vicinity of the spray while keeping the overall cell count relatively low.
2. *Fully implicit momentum coupling* – Grid convergence cannot be adequately demonstrated if running with a fine mesh causes numerical instabilities. As described in [20], previous studies suffered from such instabilities when the cell size was on the order of the nozzle diameter or smaller. The current methodology utilizes a fully implicit liquid-gas momentum coupling approach to keep the simulations stable in the presence of small cells and high liquid volume fractions. Specifically, an iterative technique is used where the drag is calculated for all drops in a cell and the gas-phase velocity is updated accordingly. This updated gas-phase velocity is used to calculate drag on all of the drops in the cell which is then used to update the gas-phase velocity. This process is repeated until the drop and gas-phase velocities converge to the specified tolerance.
3. *Improved liquid-gas coupling* – The current methodology utilizes a Taylor series expansion to calculate the gas-phase velocity in the liquid-gas coupling calculations. In this approach, the gas-phase velocity at the parcel location $u_{p,i}$ is given by

$$u_{p,i} = u_{c,i} + \left(x_{p,j} - x_{c,j}\right)\frac{\partial u_i}{\partial x_j} \tag{4}$$

where $u_{c,i}$ and $x_{c,i}$ are the cell-centered gas-phase velocity and location, respectively, and $x_{p,i}$ is the parcel location. Use of the Taylor series expansion significantly reduces grid artifacts on the spray over traditional "nearest node" coupling approaches.

Copyright © 2012 by ASME

4. *Temporal liquid mass distribution* – When refining the mesh around a spray, a common error is to keep the total number of injected parcels over the injection duration constant. This can result in the undesirable behavior of ever increasing liquid penetration from successive refinements of the mesh. When the mass in a cell is small compared to the mass of a parcel, the amount of momentum in the liquid is enough to quickly bring the cell's velocity up to the liquid velocity. As a result, there is minimal or no drag on the parcel's drops outside of the core of the spray, resulting in excessive penetration. To remedy this issue, the current approach significantly increases the injected number of parcels as the embed scale is increased (shown below in Table 4).
5. *Spatial liquid mass distribution* – Similar undesirable behavior as described above can occur when a point source injection is used with a fine mesh. In the current approach, the liquid mass is injected within a circle instead of at a point source. The radius of the circle is equal to the nozzle radius.

EXPERIMENTS FOR COMPARISON

The spray data of Margot et al. [21] is used to explore the grid convergence behavior of non-evaporating sprays. The experimental conditions examined in this work are provided in Table 1.

Vaporizing and reacting spray data for comparison are obtained from Sandia National Laboratories through the Engine Combustion Network (ECN) [22, 23, 24]. The ECN encourages collaborative efforts within the engine combustion community to develop a high-fidelity dataset for Diesel surrogates. The ECN has an internet data library on well-documented spray experiments at engine-relevant conditions in a constant-volume combustion chamber [22]. The dataset currently includes both non-reacting and reacting parameters. Recently, data on non-reacting and reacting characteristics of n-dodecane were also added [25]. The first ECN workshop focused on standardizing definitions to best capture experimental measurements of liquid length, vapor penetration, ignition delay, and flame lift-off length for the modeling community.

Fuel	Diesel
Ambient Composition	SF_6
Ambient Temperature (K)	298
Ambient Density (kg/m^3)	22
Injection Pressure (MPa)	80
Fuel Temperature (K)	363
Fuel Density (kg/m^3)	806
Nozzle Diameter (mm)	0.14
Injection Duration (ms)	1.45

Table 1: Conditions for the non-evaporating spray experiments of Margot et al. [21].

In the ECN, experiments are conducted in a constant-volume, quiescent, pre-burn-type combustion vessel to generate high-temperature and high-pressure gases to simulate the thermodynamic conditions obtained in a compression ignition engine. A premixed combustible mixture is spark-ignited, which burns to completion. The combustion products cool over a long time due to heat transfer to the vessel walls. Once the desired pressure and temperature are reached, the fuel injector is triggered and injection occurs. The conditions for the ECN data investigated in this work are noted in Table 2. Advanced optical diagnostics are used to obtain liquid and vapor penetration versus time, liquid length, ignition delay, pressure-rise rate, flame lift-off length, and quantitative soot volume fraction.

ECN Spray Case	Vaporizing Spray	Reacting Spray
Fuel	n-Dodecane	n-Heptane
Ambient Composition	0% O_2	10–21% O_2
Ambient Temperature (K)	900	800–1300
Ambient Density (kg/m^3)	22.8	14.8, 30
Injection pressure (MPa)	150	150
Fuel Temperature (K)	363	373
Nozzle diameter (mm)	0.09	0.10
Injection Duration (ms)	1.5	6.8
Mass Injected (mg)	3.5	17.8

Table 2: Conditions for the vaporizing and reacting spray experiments at Sandia National Laboratories.

RESULTS AND DISCUSSION

This section presents the results of the grid convergence studies in order of physical complexity. First, a non-evaporating spray case is simulated in order to examine the effect of mesh size on liquid penetration. Next, an evaporating spray case is used to assess the convergence behavior of vapor penetration and liquid length. Finally, the extension of spray convergence to combustion characteristics such as ignition delay and flame lift-off length is explored through a set of reacting spray cases.

In the following discussions, the computational definitions used for liquid penetration, vapor penetration, ignition delay, and flame lift-off length are presented in Table 3.

Parameter	Definition
Liquid Penetration	Axial distance encompassing 97% of the injected liquid fuel mass.
Vapor Penetration	Maximum distance from the injector where the fuel mass fraction is 0.1%.
Ignition Delay	Ignition is said to occur when T is ≥ 2000 K in a cell.
Flame Lift-off Length	Farthest upstream location of the T = 2000 K contour in the spray axial direction.

Table 3: Definitions used for the parameters of interest in the CFD simulations.

Copyright © 2012 by ASME

Non-Evaporating Sprays

As a first test of grid convergence, the non-evaporating spray experiments of Margot et al. [21] were simulated. Seven different mesh resolutions were tested in the current study. The cell sizes and corresponding embed scales are shown in Table 4. Note that the values shown in the table refer to the minimum cell sizes used for AMR as well as for fixed embedding around the injector. With a nozzle diameter d_n of 0.14 mm, embed scales of 5 and 6 correspond to multiple cells inside of the nozzle, as shown in the third column of Table 4. Finally, the number of injected parcels for each of the cases is presented in the last column of Table 4. As previously described, it is important to increase the number of injected parcels as the mesh is refined.

Embed Scale	Cell Size, dx (mm)	d_n / dx	Number of Injected Parcels
0	2.0	0.07	2,000
1	1.0	0.14	16,000
2	0.5	0.28	128,000
3	0.25	0.56	512,000
4	0.125	1.12	2,048,000
5	0.0625	2.24	8,192,000
6	0.03125	4.48	21,000,000

Table 4: AMR embed scales (first column), corresponding cell sizes (second column), number of cells inside of the nozzle diameter (third column), and number of injected parcels (last column) for the non-evaporating spray simulations.

Figure 1 shows liquid penetration as a function of time for measurements and predictions using the seven mesh resolutions defined in Table 4. It is clear from this comparison that coarse grids (i.e., 1.0 and 2.0 mm) significantly under-predict penetration in the early stages of injection and do not capture the correct behavior of penetration as a function of time. As the mesh is refined to 0.5 mm, the slope of the liquid penetration reduces as time progresses, similar to the experimental behavior. At a cell size of 0.25 mm, reasonable grid convergence is achieved with only small changes occurring for further refinement. Finally, the penetration curves for cell sizes of 0.0625 mm and 0.03125 mm are virtually identical. In addition to grid convergence, excellent agreement with the experimental measurements is achieved for cell sizes of 0.25 mm and smaller. Note that since the 2.0 mm case greatly under-predicts liquid penetration (which is expected due to severe under-resolution) it is excluded from further examination in this section.

In order to explain why grid convergence of liquid penetration is achieved, various gas-phase quantities are investigated. In particular, spray centerline velocity, turbulent kinetic energy, and turbulent viscosity are presented as functions of spray axial location in Fig. 2. The quantities are shown for a time of 0.5 ms.

As shown in Figure 2(a), velocity varies significantly as the mesh resolution changes for relatively coarse grids. An under-resolved velocity field results in an over-prediction of the liquid-gas relative velocity, which in turn produces excessive drag and drop breakup. This leads to an under-prediction of the near-nozzle penetration as shown in Fig. 1. On the other hand, as the cell size is decreased, the gas-phase velocity near the nozzle increases, resulting in lower relative velocities and less drag. For cell sizes at and below 0.125 mm, where at least one cell is included inside of the nozzle diameter (see Table 4), the gas-phase velocity approaches the liquid injection velocity. This results in a negligible relative velocity in the core of the spray with minimal drag, leading to accurate predictions of near nozzle liquid penetration.

Figure 2 clearly indicates that convergence in the gas-phase velocity is seen for cell sizes below 0.125 mm. However, Fig. 1 shows that even a cell size of 0.25 mm, which somewhat under-predicts the near nozzle gas-phase velocity, is adequate to reasonably predict liquid penetration. This result is due to the fact that the downstream penetration is highly dependent on the turbulence field.

Similar to velocity, turbulent kinetic energy and turbulent viscosity are significantly under-predicted for relatively coarse grids. On the other hand, as the mesh is refined to 0.25 mm, the appropriate turbulence scales start to become resolved and the turbulence field begins to converge. In fact, the centerline turbulent viscosity for cell sizes of 0.25 mm down to 0.03125 mm is very similar, as shown in Fig. 2(c).

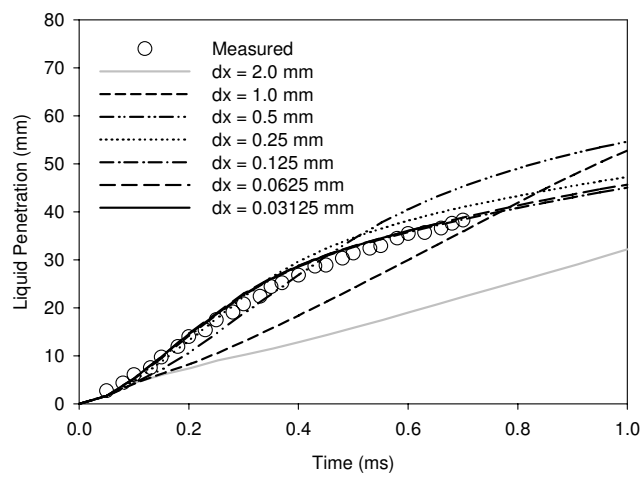

Figure 1: Comparison of measured and predicted liquid penetration for the non-evaporating spray case. Seven predicted curves are presented for the cell sizes given in Table 4.

Copyright © 2012 by ASME

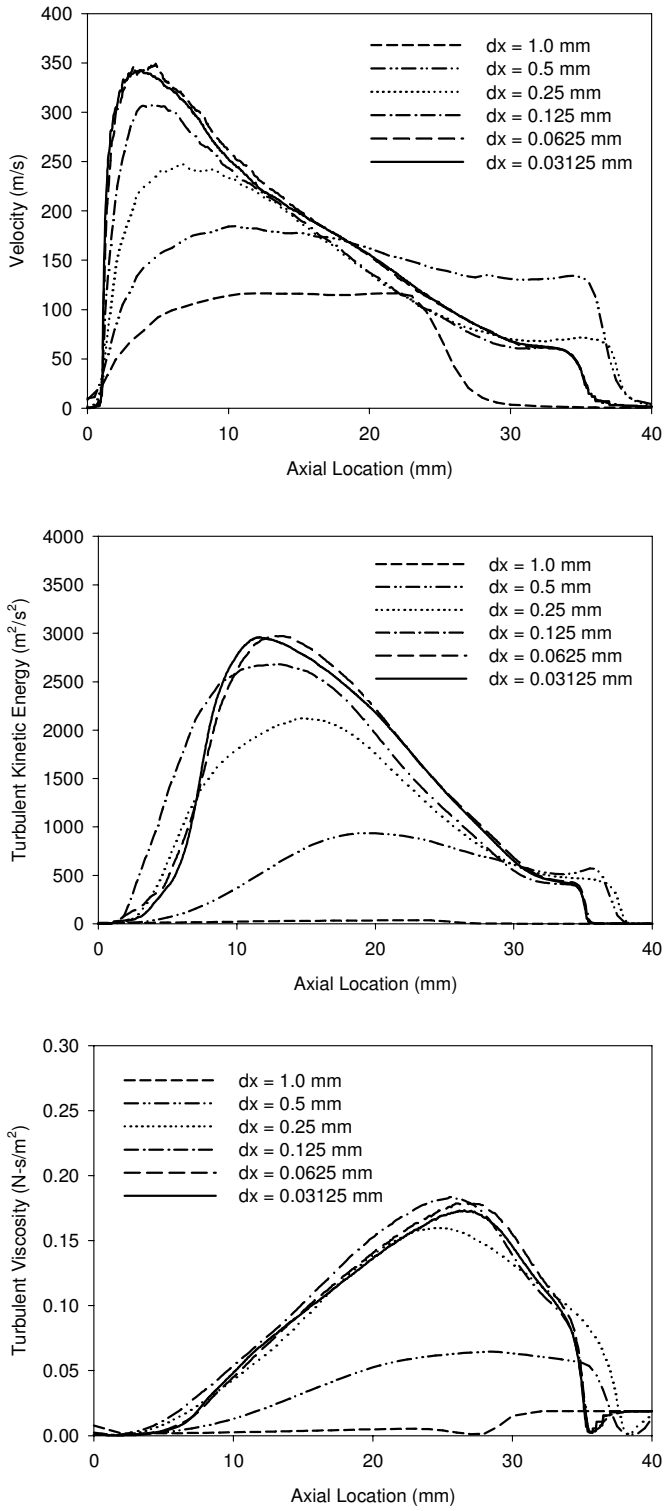

Figure 2: Comparison of spray centerline (a) velocity, (b) turbulent kinetic energy, and (c) turbulent viscosity for a range of mesh resolutions. The results are given for a time of 0.5 ms.

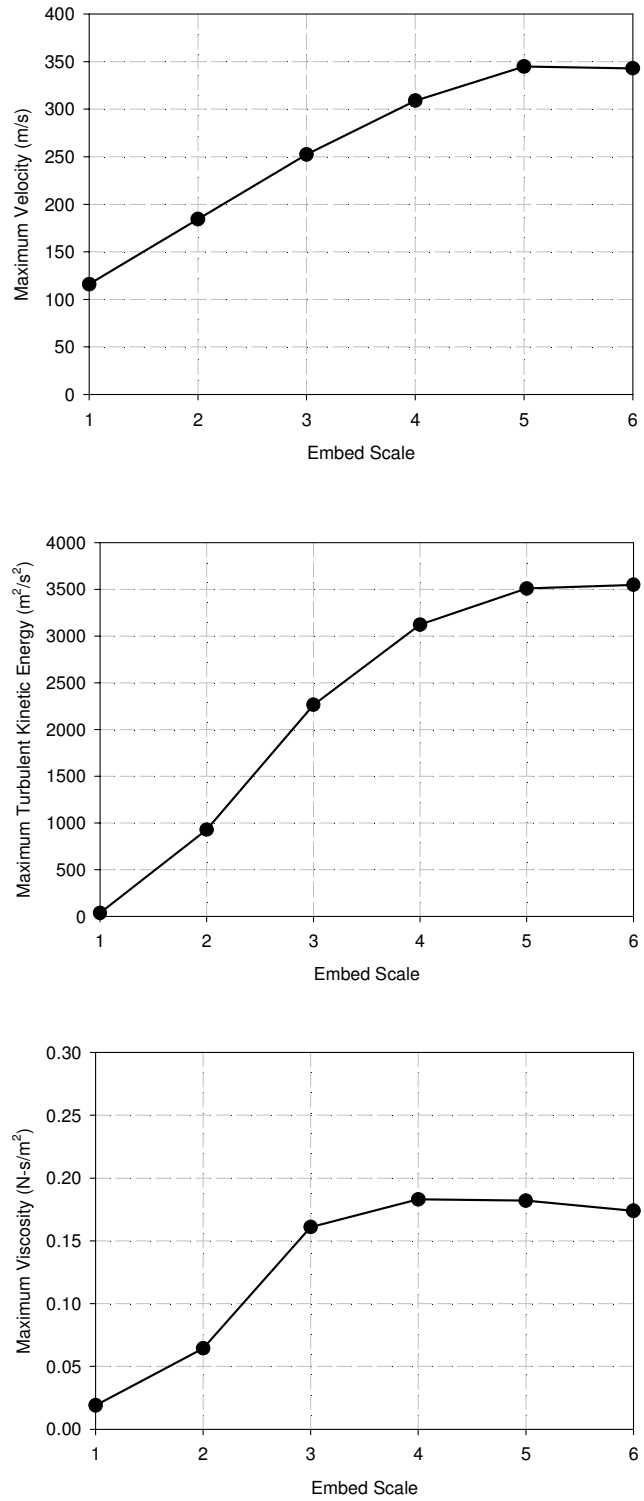

Figure 3: Comparison of maximum (a) velocity, (b) turbulent kinetic energy, and (c) turbulent viscosity for a range of embed scales. Note that an embed scale of 1 gives a cell size of 1.0 mm while an embed scale of 6 gives a cell size of 0.03125 mm. The results are given for a time of 0.5 ms.

Copyright © 2012 by ASME

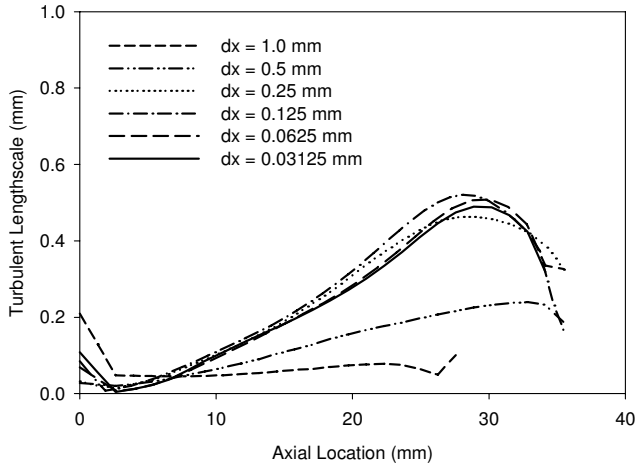

Figure 4: Comparison of spray centerline turbulent length-scales for a range of mesh resolutions. The results are given for a time of 0.5 ms.

In order to further illustrate grid convergence, the maximum gas-phase velocity, turbulent kinetic energy, and turbulent viscosity as functions of embed scale (the corresponding cell sizes are shown in Table 4) are presented in Fig. 3 for a time of 0.5 ms. Note that it was verified that the maximum values occur in the vicinity of the spray for all cases. The plots show that while the maximum velocity and turbulent kinetic energy display convergence at an embed scale of 5 (i.e., cell size of 0.0625 mm), the maximum turbulent viscosity reasonably converges at an embed scale of 3 (0.25 mm cells). Recall from Fig. 1 that the predicted liquid penetration displayed reasonable grid-convergence at a cell size of 0.25 mm.

Figure 4 shows the turbulent length-scale as a function of spray axial location at a time of 0.5 ms. Here the turbulent length-scale is given by

$$l_t = \left(\nu_t^3/\varepsilon\right)^{1/4} = C_\mu^{3/4} k^{3/2}/\varepsilon \qquad (5)$$

where $\nu_t = C_\mu \left(k^2/\varepsilon\right)$ and $C_\mu = 0.0845$ for the RNG $k-\varepsilon$ model. In this plot, the predicted values have been clipped near the downstream location where the liquid spray ends as the ambient length-scales are not of interest for this discussion. The above length-scale is an indication of the smallest scales in the simulation.

From Fig. 4 it is clear that the length-scale achieves reasonable grid-convergence for a cell size of 0.25 mm, similar to turbulent viscosity. Note that the length-scales predicted for the coarse grids (1.0 mm and 0.5 mm) are significantly lower than the cell sizes used for these cases. It is therefore understandable that these solutions are not converged due to the lack of resolving the smallest scales. On the other hand, the converged length-scale varies from close to zero to about 0.5 mm, depending on the axial spray location. As a result, cells of 0.25 mm and smaller are below the size of the turbulent length-scales throughout much of the spray, indicating that the important scales are resolved. It is believed that this is the primary reason that the liquid penetration shows reasonable convergence at a cell size of 0.25 mm.

As a final step in examining grid convergence of the non-vaporizing case, the computational grids and predicted spray shapes are provided in Fig. 5 for a time of 0.5 ms (only a single time is shown for brevity). Note that the cases shown in Figs. 5(a) – 5(e) have a base mesh size of 2.0 mm, while the case in Fig. 5(f) has a base mesh size of 1.0 mm. This reduction in base mesh for the finest resolution (i.e., 0.03125 mm) is done only to maximize the efficiency of parallel processing and has no effect on the results.

From Fig. 5 it is clear that velocity AMR is correctly adding mesh resolution around the spray where it is needed. In addition, the axial view spray images show that although coarser grids can lead to mesh artifacts (i.e., the "clover" effect seen for cell sizes of 1.0 and 0.5 mm), this undesirable behavior tends to go away as the mesh is refined. Finally, the images are further confirmation of the grid convergence behavior exhibited in the line plots. It is clear that the sprays look very similar for cell sizes below 0.125 mm, while a cell size of 0.25 mm produces reasonably grid convergent results. Note that for the finest resolutions, several droplets are observed outside of the bulk spray. These droplets have been verified to have negligible mass and are present as an artifact of injecting a higher number of parcels with increasing grid resolution.

It should be noted that a common rule-of-thumb for Lagrangian spray models is to require that the liquid volume is less than 10% of the gas-phase cell volume. In the literature, this restriction is often attributed to the so-called "dilute assumption" in the spray equation formulation [26]. However, Subramaniam showed that the spray equation can be derived without this assumption and that it has no theoretical basis [27]. On the other hand, as noted in [20], significant numerical stability problems can occur with large liquid volume fractions. As previously mentioned, the current approach couples the Lagrangian and Eulerian momentum in a fully implicit fashion to allow for very small cells with high liquid volume fractions without suffering stability issues.

Figure 6 shows spray centerline liquid volume fraction as a function of axial location. Here the liquid volume fraction is defined as the total liquid volume in a cell divided by the cell volume. It can be seen that for cell sizes of 0.25 mm and larger, the liquid volume fraction is below 0.1, even close to the nozzle exit. As the mesh is refined to 0.125 mm, the liquid volume fraction exceeds 0.2 close to the nozzle exit. For cell sizes below 0.125 mm the liquid volume fraction is close to 1.0 near the nozzle exit, but quickly drops to below 0.2 by about 3 mm downstream.

There are two important points to note from the current results with respect to liquid volume fraction. First of all, even with a liquid volume fraction well above 0.1 for some of the cases, all of the simulations remained numerically stable. Secondly, if violating the 10% rule-of-thumb near the nozzle

Copyright © 2012 by ASME

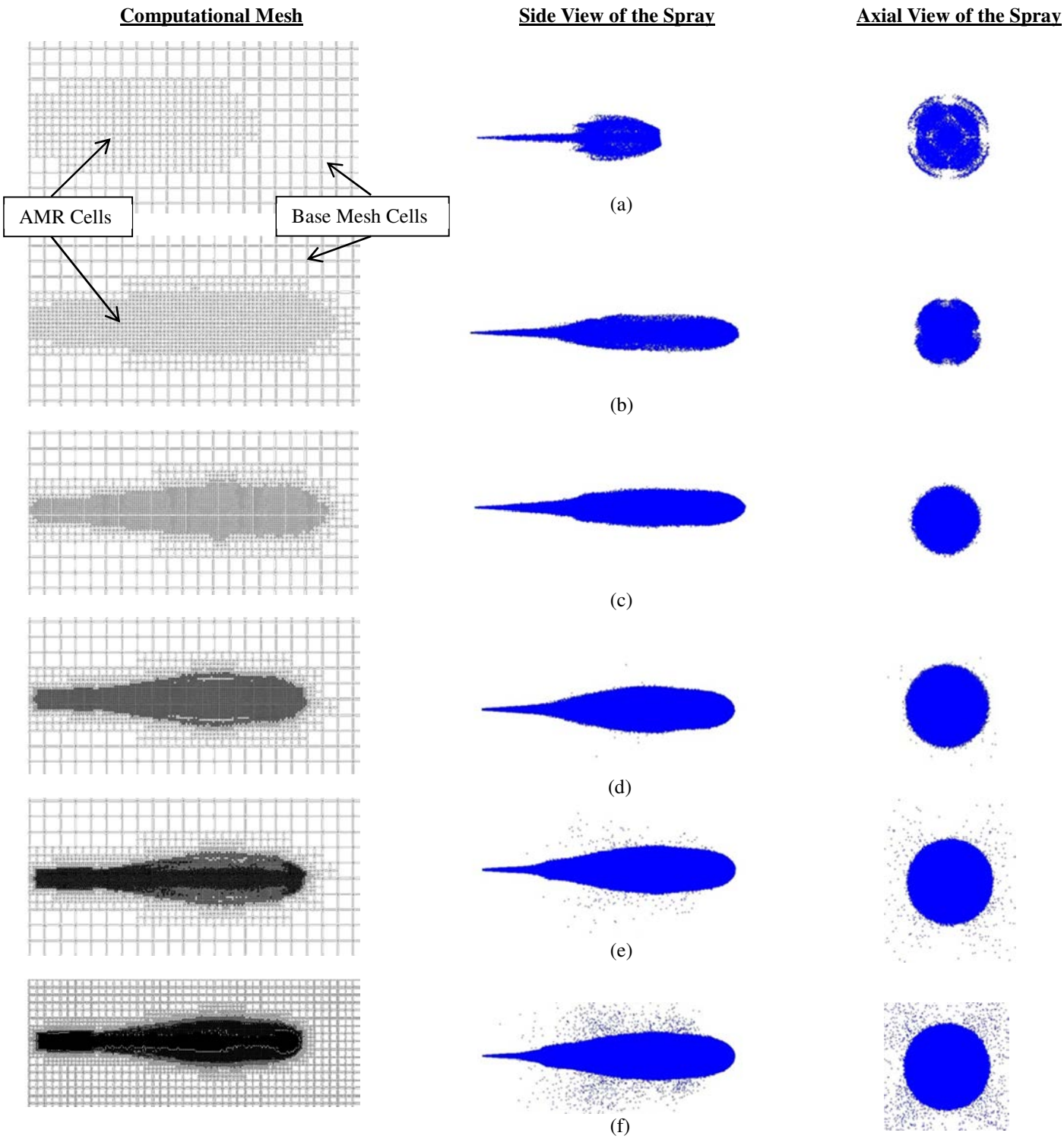

Figure 5: Comparison of computational mesh (left), side view of the spray (middle), and axial view of the spray (right) for velocity AMR cell sizes of (a) 1.0 mm, (b) 0.5 mm, (c) 0.25 mm, (d) 0.125 mm, (e) 0.0625 mm, and (f) 0.03125 mm. The results are given for a time of 0.5 ms.

Copyright © 2012 by ASME

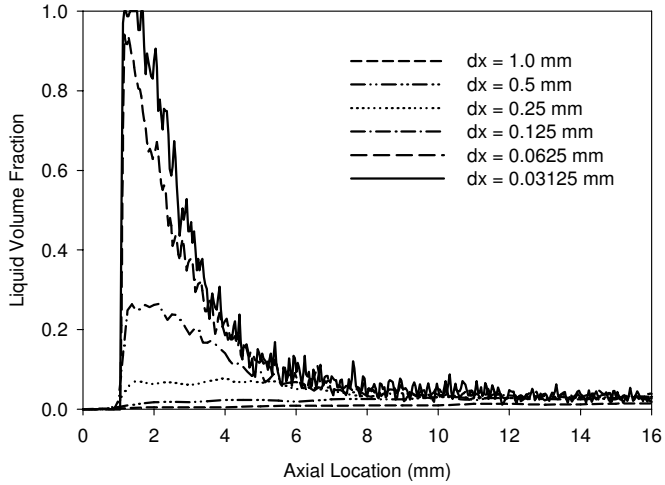

Figure 6: Comparison of liquid volume fraction as a function of axial location for a range of mesh resolutions. The results are given for a time of 0.5 ms. Note that the nozzle exit is at an axial location of 1 mm.

was truly a significant problem, the current results would not exhibit grid convergence. The answers with cell sizes below 0.25 mm are very similar to the 0.25 mm case, where the liquid volume fraction is always below 0.1. It could be argued that some of the models are not appropriate for large liquid volume fractions due to limitations in the correlations on which they are based [27], however the area where this is a concern is minimized by injecting a large number of liquid parcels over a spatial distribution. Note that the liquid volume fraction is only large near the nozzle, resulting in near zero drag in the core of the spray which is the desired behavior.

Vaporizing Sprays

As a further test of grid convergence, the vaporizing n-dodecane spray case known as "Spray A" from the Engine Combustion Network (ECN) was investigated. The experimental conditions for this case were provided in Table 2.

Similar to the non-evaporating spray case, seven different mesh resolutions were simulated. The cell sizes and corresponding embed scales for velocity AMR are identical to those given in Table 4. Note however that the ratios of nozzle diameter to cell sizes are different for this case as a smaller hole size was used.

Figure 7 shows a comparison of measured and predicted liquid penetration for Spray A. The predictions include results from the seven different mesh resolutions given in Table 4. As this is an evaporating case, the measured liquid penetration increases until it reaches a quasi-steady liquid length. This behavior is reproduced in the predictions for all mesh sizes, however the coarse grids significantly over-predict the liquid length. For cell sizes of 0.25 mm and finer the liquid length is accurately captured.

Grid convergence of liquid length is more clearly presented in Fig. 8. In this plot, the quasi-steady liquid length is plotted as a function of embed scale, where an embed scale of 1 corresponds to a cell size of 1.0 mm and an embed scale of 6 corresponds to a cell size of 0.03125 mm. It is clear that the liquid length exhibits grid convergent behavior, with reasonable accuracy starting at an embed scale of 3 (i.e., cell sizes of 0.25 mm).

In addition to liquid length data, fuel vapor penetration measurements are also available for this case and are shown in Fig. 9. The predicted vapor penetration is also shown over the range of mesh resolutions examined. It is clear from this figure that vapor penetration exhibits grid convergent behavior, with each refinement resulting in a smaller difference in penetration compared to the previous refinement. It is also apparent that, although the early predicted vapor penetration agrees well with the measurements for fine grids, the later part of the penetration converges to values noticeably lower than the measurements. This may be due to uncertainties in the experimental conditions.

Finally, in order to assess spatial convergence of the vapor field, the spray centerline fuel mass fraction is compared for the range of mesh resolutions. The results are shown in Fig. 10 for a time of 1.5 ms, which corresponds to the end of fuel injection. Very similar fuel mass fraction profiles are achieved when cell sizes of 0.25 mm or finer are used. A cell size of 0.5 mm maintains the general behavior of the profile, but with a lower predicted maximum value. The profiles for cell sizes of 1.0 and 2.0 mm look completely different from those for the finer grids and are believed to be inaccurate.

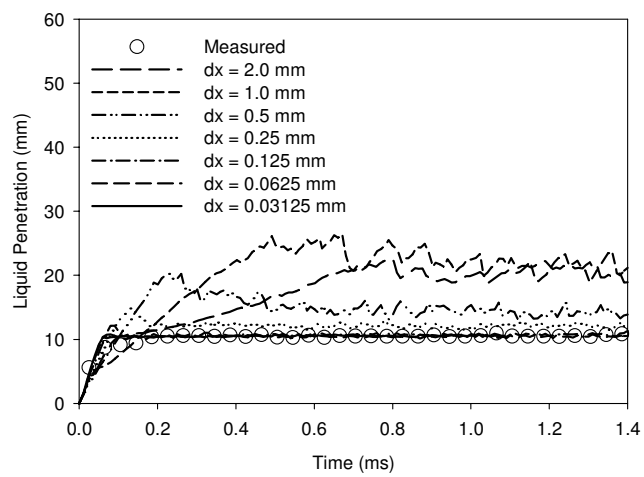

Figure 7: Comparison of measured and predicted liquid penetration for the Spray A evaporating spray case. Seven predicted curves are presented for the cell sizes given in Table 4.

Copyright © 2012 by ASME

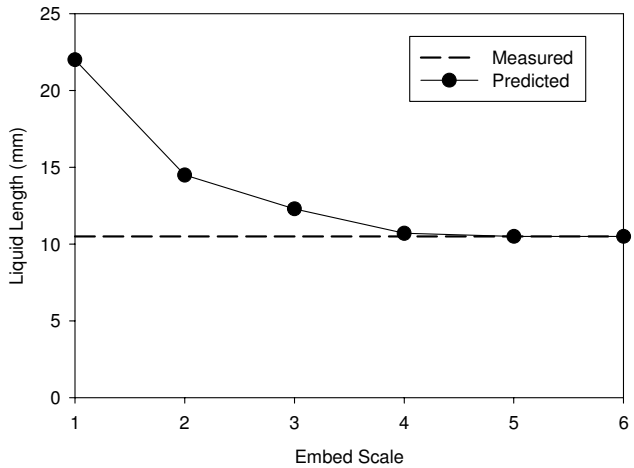

Figure 8: Comparison of measured and predicted liquid length for the Spray A evaporating spray case. The predictions are shown for a range of embed scales.

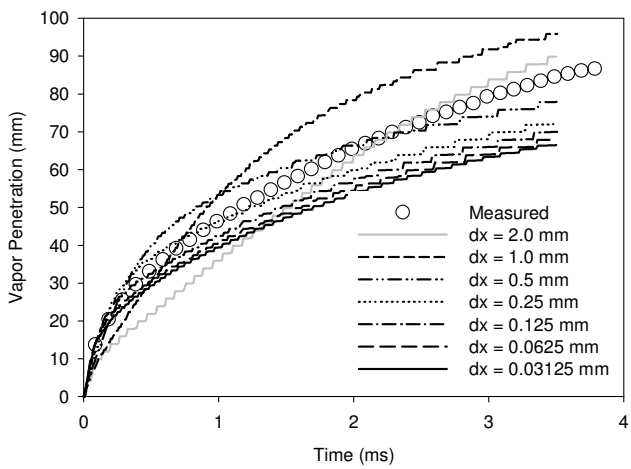

Figure 9: Comparison of measured and predicted vapor penetration for the Spray A evaporating spray case. Seven predicted curves are presented for the cell sizes given in Table 4.

Reacting Sprays

This section extends the spray convergence studies by examining the influence of cell size under combusting spray conditions. The experimental data is available through the ECN from Sandia National Laboratory [22, 23, 24]. Simulations were performed with a reduced n-heptane mechanism consisting of 42 species and 168 reactions obtained from Chalmers University [19]. In addition, the well-mixed assumption is employed and hence models for sub-grid scale turbulence-chemistry interactions are not included. As the reacting spray simulations include detailed chemistry calculations, the very fine mesh resolutions of 0.0625 and 0.03125 mm are not considered in order to keep the simulation runtimes reasonable. In addition, a 2 mm mesh proved to be

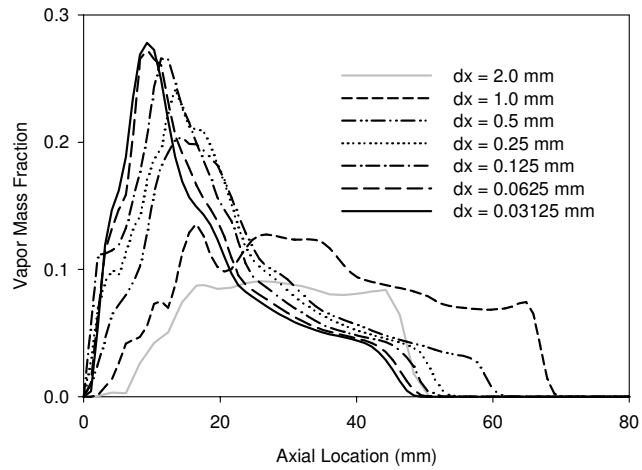

Figure 10: Comparison of spray centerline vapor mass fraction for a range of mesh resolutions. The results are given for a time of 1.5 ms.

considerably too coarse in the non-reacting simulations and is thus also not considered in the combusting spray simulations. As a result, AMR cell sizes of 1 mm, 0.5 mm, 0.25 mm, and 0.125 mm were considered in this section. Figures 11 and 12 show the effect of ambient oxygen concentration on ignition delay and flame lift-off length. With increasing ambient oxygen concentration, both the ignition delay and flame lift-off length decrease. This is due to the fact that the flame reactivity is enhanced. Simulations with all grid sizes can capture this trend qualitatively well. Discrepancies in ignition delay at lower oxygen concentrations are attributed to deficiencies in the chemical kinetic mechanism and are consistent with earlier studies in the literature [28, 29]. In general, with a decrease in cell size, flame lift-off length is observed to increase for all oxygen concentrations, however, no such trends are observed with respect to ignition delay. The differences in ignition delay and flame lift-off length values between the 0.125 mm and 0.25 mm grids are lower than ± 1% and ± 3% respectively, indicating reasonable grid convergence.

Figures 13 and 14 present axial ignition location and liquid length as a function of oxygen concentration for the four different grid sizes. Since experimental data is not available for these parameters, the plots are only presented to further demonstrate grid convergence. The axial location of ignition does not show any trend with different cell sizes which is not surprising since there were also no trends observed for ignition delay (see Fig. 11). Liquid length is observed to decrease with decreasing cell sizes. It should be noted that for all cell sizes other than 1 mm, the liquid length is lower than the flame lift-off length. This represents minimal spray-flame interactions [30, 31]. However, for the largest grid size of 1 mm, at an ambient oxygen concentration of 21%, the liquid length is

Copyright © 2012 by ASME

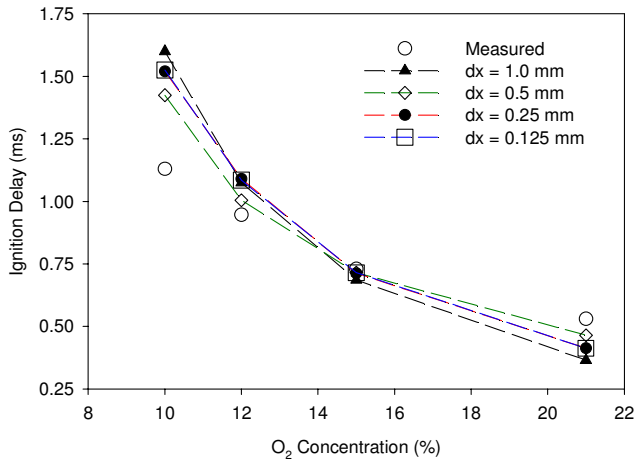

Figure 11: Influence of mesh size on ignition delay at different ambient oxygen concentrations, compared with Sandia measurements for an ambient density of 14.8 kg/m^3 and a temperature of 1000 K.

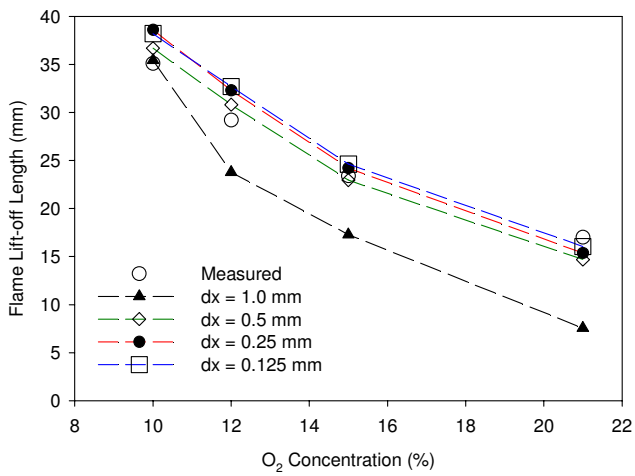

Figure 12: Influence of mesh size on flame lift-off length at different ambient oxygen concentrations, compared with Sandia measurements for an ambient density of 14.8 kg/m^3 and a temperature of 1000 K.

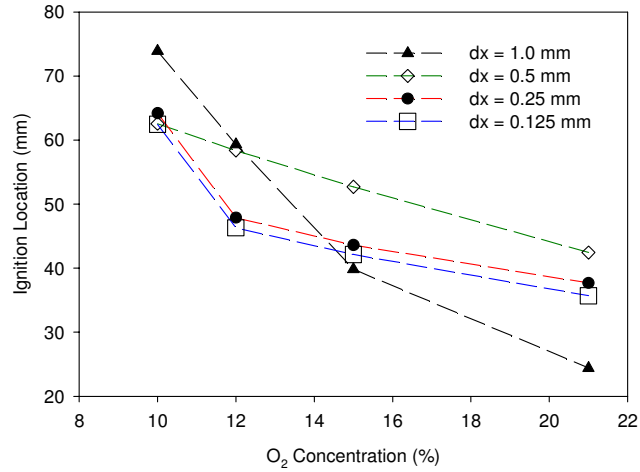

Figure 13: Influence of mesh size on axial location of ignition at different ambient oxygen concentrations for an ambient density of 14.8 kg/m^3 and a temperature of 1000 K.

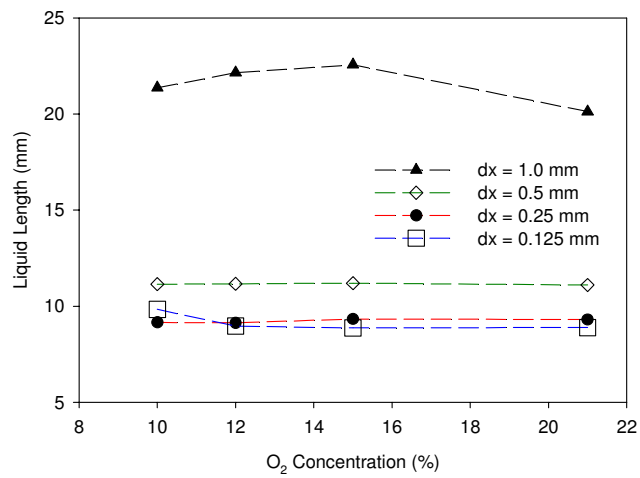

Figure 14: Influence of mesh size on liquid length at different ambient oxygen concentrations for an ambient density of 14.8 kg/m^3 and a temperature of 1000 K.

higher than the flame lift-off length, which can result in enhanced spray-flame interactions. The differences in axial ignition location and liquid length values between 0.125 mm and 0.25 mm grids are lower than ± 5% and ± 6%, respectively.

Figure 15 presents the influence of grid size on the temperature, OH mass fraction, and equivalence ratio contours for the reacting spray cases at an ambient oxygen concentration of 21%. The field of view in these images is 85 mm x 25 mm in the axial and radial directions, respectively. Due to the axi-symmetric nature of the spray and combustion processes, images are presented on a cut-plane through the center of the fuel jet. The flame structure in terms of temperature, OH mass fraction and equivalence ratio is distinctly different between the 1 mm case and the other grid sizes. The flame is observed to propagate further upstream and the flame length is also longer for the 1 mm case. This represents higher reactivity which is not surprising since the ignition delay was observed to be lower for this case (see Fig. 11). In general, the flame length is seen to decrease with decreasing cell size. The contour plots of 0.25 mm and 0.125 mm cases look quite similar, further demonstrating grid convergence.

Copyright © 2012 by ASME

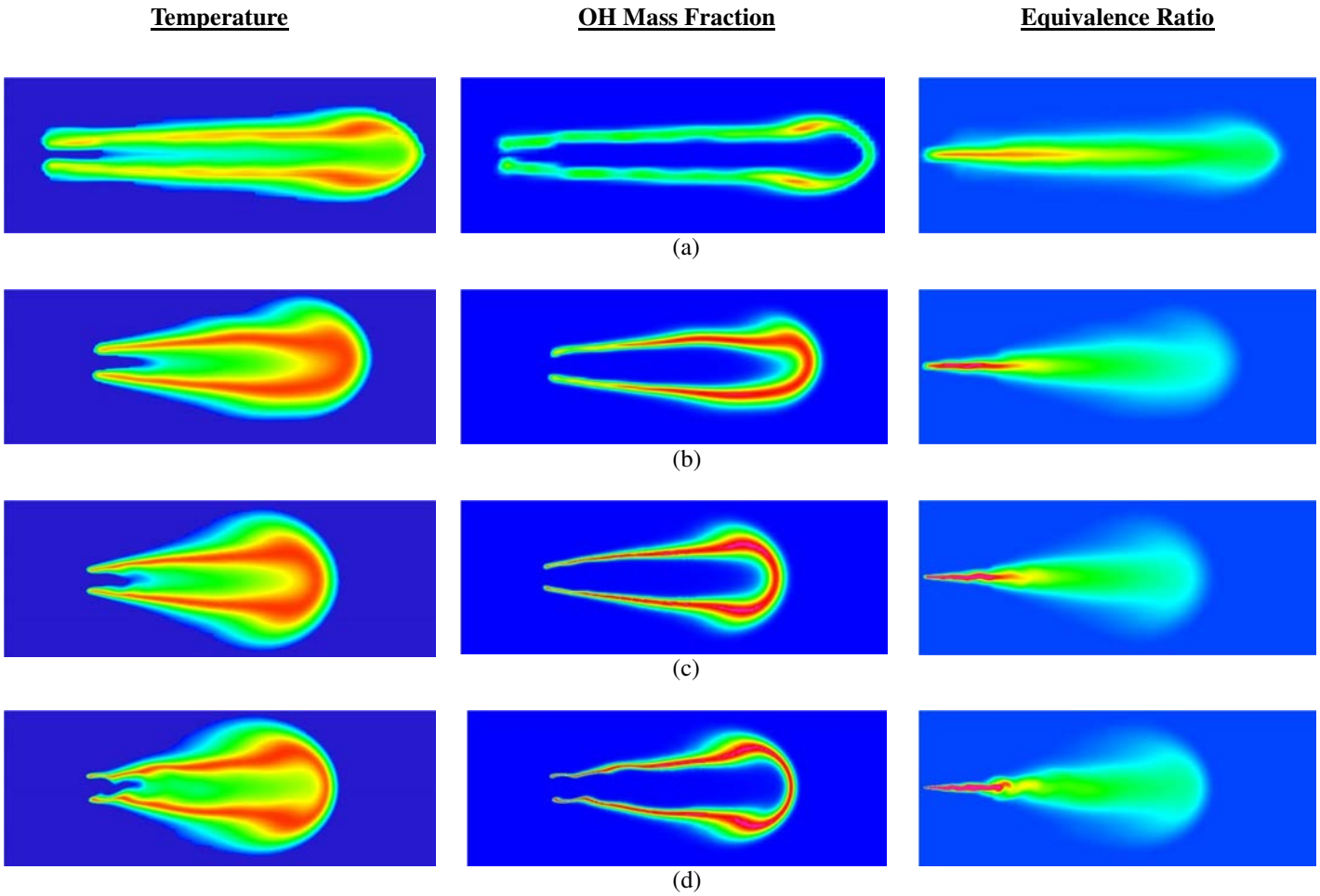

Figure 15: Comparison of temperature (left), OH mass fraction (middle), and equivalence ratio (right) for velocity AMR cell sizes of (a) 1.0 mm, (b) 0.5 mm, (c) 0.25 mm, and (d) 0.125 mm. The results are given for an oxygen concentration of 21% at 1.5 ms after the start of injection.

Recommended Cell Sizes for Spray Calculations

The previous sections have demonstrated grid convergence for a number of different spray scenarios, ranging from a non-evaporating case to reacting cases. Since convergence was achieved, it is now possible to recommend cell sizes based on accuracy/runtime tradeoffs. This section focuses on the vaporizing and reacting cases as they include the phenomena of interest in engine simulations.

Table 5 includes the maximum cell count and wall-clock times for the seven mesh sizes simulated for the vaporizing spray case. The number of processors is also presented, as this varied between cases. As shown in the table, the finest resolution case, which included a maximum cell count of over four million cells, required over seven days of runtime on 32 processors. It is important to note that the increased runtime for finer grids is not only due to the number of cells in the computational domain. The increased number of injected spray parcels and reduced numerical time-steps needed to maintain CFL restrictions are also large contributors to the overall runtime.

The computational times and the maximum cell counts for the four reacting spray cases are also presented in Table 6. In this case, the largest runtime is 250 hours for the 0.125 mm case.

Cell Size, dx (mm)	Maximum Cell Count	Run Time (hours)	Number of Processors
2.0	134,000	0.13	16
1.0	151,000	0.17	16
0.5	185,000	0.33	16
0.25	252,000	0.94	16
0.125	445,000	3.28	16
0.0625	1,030,000	13.9	32
0.03125	4,420,000	182.0	32

Table 5: Maximum cell count and wall-clock run times for the seven different grid sizes studied in the vaporizing spray simulations. The simulations were stopped at 3.5 ms after the start of injection.

Copyright © 2012 by ASME

Cell Size, dx (mm)	Maximum Cell Count	Run Time (hours)	Number of Processors
1.0	80,000	1.75	24
0.5	260,000	13.5	24
0.25	390,000	70.0	24
0.125	760,000	250.0	24

Table 6: Maximum cell count and wall-clock run times for the four different grid sizes studied in the reacting spray simulations. The simulations were stopped at 2.5 ms after the start of injection.

Figure 16 shows wall-clock time as a function of embed scale for the vaporizing and reacting spray cases. This plot can be used, along with the convergence results, to determine appropriate cell sizes keeping in mind both accuracy and computational cost. For the vaporizing spray case it was shown that reasonable grid convergence was achieved for an embed scale of 3 (cell size of 0.25 mm). As shown in Fig. 16, this is well before the "knee" in the curve at an embed scale of 5. On the other hand, the knee in the reacting spray curve occurs for a smaller embed scale in the area of 2 or 3. Similar to the vaporizing spray cases, reasonable grid convergence is seen for an embed scale of 3 for the reacting cases with a runtime that is about a factor of 3.5 lower than an embed scale of 4. The results suggest that an embed scale of 3, or cell size of 0.25 mm, is optimum for the current simulations keeping in mind both accuracy and computational cost. To speed-up the runtime for the 0.25 mm reacting case, a simulation using the recently implemented multi-zone chemistry solver [32] was performed. The multi-zone solver significantly speeds up combustion calculations by grouping cells with similar properties into zones in the chemistry calculations. The multi-zone simulation ran in about 12 hours, giving a 6 times speed-up over the full SAGE simulation. Thus, a reasonable runtime is achieved incorporating detailed chemistry with a cell size of 0.25 mm.

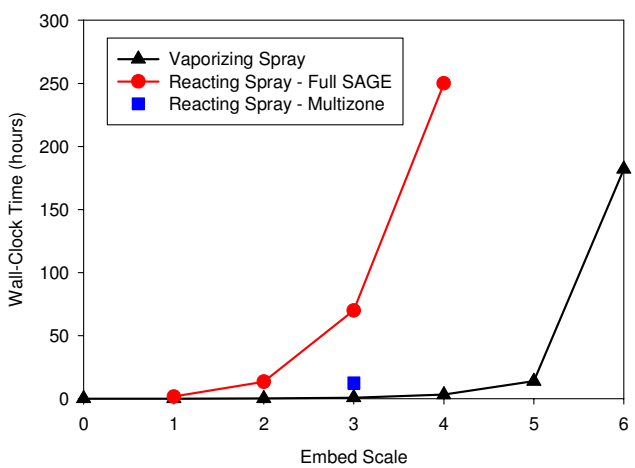

Figure 16: Wall-clock time as a function of embed scale for the vaporizing and reacting spray cases.

CONCLUSIONS

This study focused on demonstrating the grid convergence of several key parameters using a state-of-the-art spray modeling methodology. The following conclusions can be made based on the results of this study:

1. Grid convergence, and not grid independence, should be the goal of modern, state-of-the-art spray models.
2. Grid convergence should be checked in order to have confidence in the results of spray simulations.
3. Grid convergence was demonstrated with the current spray models for key parameters of interest in both non-reacting and reacting spray simulations.
4. Cell sizes down to 30 microns (i.e., 0.03125 mm) were simulated, verifying the robustness of the current spray model.
5. Grid-convergent models allow researchers to make recommendations on appropriate cell sizes that optimize the accuracy/runtime tradeoff.
6. In the current work, with AMR, a cell size of 0.25 mm is proposed for RANS-based spray simulations. This resolution gives both reasonable accuracy and acceptable runtimes for the cases investigated here.

ACKNOWLEDGMENTS

The submitted manuscript has been created in collaboration with UChicago Argonne, LLC, operator of Argonne National Laboratory (Argonne). Argonne, a U.S. Department of Energy Office of Science laboratory, is operated under Contract No. DE-AC02-06CH11357. The U.S. Government retains for itself, and others acting on its behalf, a paid-up, nonexclusive, irrevocable worldwide license in said article to reproduce, prepare derivative works, distribute copies to the public, and perform publicly and display publicly, by or on behalf of the Government.

REFERENCES

1. Yang, X., Takamoto, Y., and Okajima, A., "Improvement of Three-Dimensional Diesel Spray Modeling in Near Region with Coarse Mesh," *SAE 2000-01-0274*, 2000.
2. Yang, X., Takamoto, Y., Okajima, A., Obokata, T., and Long, W., "Comparison of Computed and Measured High-Pressure Conical Diesel Sprays," *SAE 2000-01-0951*, 2000.
3. Abani, N., Munnannur, A., Reitz, R. D., "Reduction of Numerical Parameter Dependencies in Diesel Spray Models," *Journal of Engineering for Gas Turbines and Power*, **130**, 2008.
4. Lippert, A. M., Chang, S., Are, S., and Schmidt, D. P., "Mesh Independence and Adaptive Mesh Refinement for Advanced Engine Spray Simulations," *SAE 2005-01-0207*, 2005.
5. Richards, K. J., Senecal, P. K., and Pomraning, E., CONVERGE (Version 1.4.1) Manual, Convergent Science, Inc., Middleton, WI, 2012.
6. Senecal, P. K., Richards, K. J., Pomraning, E., Yang, T., Dai, M. Z., McDavid, R. M., Patterson, M. A., Hou, S., and

Copyright © 2012 by ASME

Shethaji, T., "A New Parallel Cut-Cell Cartesian CFD Code for Rapid Grid Generation Applied to In-Cylinder Diesel Engine Simulations," *SAE 2007-01-0159*, 2007.
7. Pomraning, E., "Development of Large Eddy Simulation Turbulence Models," Ph.D. Thesis, University of Wisconsin-Madison, 2000.
8. Leonard, A., "Energy Cascade in Large-Eddy Simulations of Turbulent Fluid Flows," *Advances in Geophysics A*, **18**, 237-248, 1974.
9. Yeo, W. K., "A Generalized High Pass/Low Pass Averaging Procedure for Deriving and Solving Turbulent Flow Equations," Ph.D. Thesis, The Ohio State University, 1987.
10. Rhie, C. M. and Chow, W. L., "Numerical Study of the Turbulent Flow Past an Airfoil with Trailing Edge Separation," *AIAA J.,* **21**, 1525-1532, 1983.
11. Issa, R. I., "Solution of the Implicitly Discretised Fluid Flow Equations by Operator-Splitting," *Journal of Computational Physics*, **62**, 1985.
12. Yakhot, V. and Orszag, S. A., "Renormalization Group Analysis of Turbulence. I. Basic Theory," *J. Sci. Comput*., **1**, 3, 1986.
13. Reitz, R. D. and Diwakar, R., "Structure of High-Pressure Fuel Sprays," *SAE 870598*, 1987.
14. Schmidt, D. P. and Rutland, C. J., "A New Droplet Collision Algorithm," *Journal of Computational Physics*, **164**, 62-80, 2000.
15. Post, S. L. and Abraham, J., "Modeling the Outcome of Drop-Drop Collisions in Diesel Sprays," *International Journal of Multiphase Flow*, **28**, 997-1019, 2002.
16. Liu, A. B., Mather, D. K., and Reitz, R. D., "Modeling the Effects of Drop Drag and Breakup on Fuel Sprays," *SAE 930072*, 1993.
17. Amsden, A. A., O'Rourke, P. J., and Butler, T. D., "KIVA-II: A Computer Program for Chemically Reactive Flows with Sprays," Los Alamos National Laboratory Report No. LA-11560-MS, 1989.
18. Senecal, P. K., Pomraning, E., Richards, K. J., Briggs, T. E., Choi, C. Y., McDavid, R. M. and Patterson, M. A., "Multi-Dimensional Modeling of Direct-Injection Diesel Spray Liquid Length and Flame Lift-Off Length Using CFD and Parallel Detailed Chemistry," *SAE 2003-01-1043*, 2003.
19. Nordin, N., "Numerical Simulations of Non-Steady Spray Combustion Using a Detailed Chemistry Approach," Thesis for the degree of Licentiate of Engineering, Dept. of Thermo and Fluid Dynamics, Chalmers University of Technology, Goteborg, Sweden, 1998.
20. Abraham, J., "What is Adequate Resolution in the Numerical Computations of Transient Jets?" *SAE 970051*, 1997.
21. Margot, X., Payri, R., Gil, A., Chavez, M., and Pinzello, A., "Combined CFD-Phenomenological Approach to the Analysis of Diesel sprays under Non-Evaporative Conditions," *SAE 2008-01-0962*, 2008.
22. http://www.sandia.gov/ecn/
23. Pickett, L. M., Genzale, C. L., Bruneaux G., Malbec, L. M., Hermant, L., Christiansen, C., and Schramm, J., "Comparison of Diesel Spray Combustion in Different High-Temperature, High-Pressure Facilities," *SAE 2010-01-2106*, 2010.
24. Pickett, L. M., Manin, J., Genzale, C. L., Siebers, D. L., Musculus, M. P. B., and Idicheria, C. A., "Relationship Between Diesel Fuel Spray Vapor Penetration/Dispersion and Local Fuel Mixture Fraction," *SAE 2011-01-0686*, 2011.
25. http://www.sandia.gov/ecn/proceed/proceedECN1.php
26. Williams, F. A., "Spray Combustion and Atomization," *Phys. Fluids*, **1**, 541, 1958.
27. Subramaniam, S., "Lagrangian-Eulerian Methods for Multiphase Flows," *Prog. Energy Combust Sci.* (in review).
28. Som, S., Aggarwal, S.K., 2010, "Effects of primary breakup modeling on spray and combustion characteristics of compression ignition engines", Combustion and Flame, Vol. 157, pp.1179-1193.
29. Som, S., 2009, "Development and Validation of Spray Models for Investigating Diesel Engine Combustion and Emissions;" PhD thesis, University of Illinois at Chicago.
30. Higgins, B. S. and Siebers, D. L., "Measurement of the Flame Lift-off Location on DI Diesel Sprays Using OH Chemiluminescence." *SAE 2001-01-0918*, 2001.
31. Siebers, D. L. and Higgins, B.S., "Flame Lift-off on Direct-Injection Diesel Sprays under Quiescent Conditions," *SAE 2001-01-0530*, 2001.
32. Raju, M., Wang, M., Dai, M., Piggott, W., and Flowers, D., "Acceleration of Detailed Chemical Kinetics Using Multi-zone Modeling for CFD in Internal Combustion Engine Simulations," *SAE 2012-01-0135*, 2012.

Copyright © 2012 by ASME